

A Novel Approach to Neutrino-Hydrogen Measurements

H. Duyang, B. Guo, S.R. Mishra and R. Petti

*Department of Physics and Astronomy,
University of South Carolina, Columbia, South Carolina 29208, USA*

Abstract

The limited statistics of the available (anti)neutrino-hydrogen interactions has been a longstanding impediment for neutrino physics. We propose a practical way to achieve accurate (anti)neutrino-hydrogen measurements, solving the principal limitations of earlier experiments. Interactions on hydrogen are extracted by subtracting measurements on thin dedicated graphite (pure C) and polypropylene (CH₂) targets within a highly segmented low-density detector. A statistics of $\mathcal{O}(10^6)$ can be realistically achieved for the various $\nu(\bar{\nu})$ -H event topologies, with efficiencies exceeding 90% and purities around 80-95%. The availability of such samples allows a determination of neutrino and antineutrino fluxes with precisions better than 1% using conventional wide-band beams. Furthermore, by contrasting these samples to corresponding measurements on heavy materials, initial and final state nuclear effects can be directly constrained in a model-independent way. The systematic uncertainties associated with both the fluxes and the nuclear smearing are crucial for long-baseline neutrino oscillation experiments. (Anti)neutrino-hydrogen interactions also provide an ideal tool for a wide range of precision tests of fundamental interactions.

PACS numbers: 13.60.Hb, 12.38.Qk

I. INTRODUCTION

To collect a large statistics neutrino experiments typically use massive nuclear targets, which are particularly relevant in long-baseline oscillation experiments due to the reduced flux at the far site [1, 2]. An understanding of the structure and interactions of hadrons within the nuclear targets is, therefore, crucial to achieve accurate measurements of neutrino interactions. The existing uncertainties in the modeling of the nuclear effects, which modify the neutrino cross-sections, as well as the final state interactions within the nucleus are not adequate to meet the precisions required by next-generation neutrino experiments [3].

Modern (anti)neutrino beams can deliver high intensity fluxes alleviating one of the primary limitations of past experiments. This progress allows the use of high resolution detectors with a relatively small fiducial mass of a few tons to obtain a more accurate reconstruction of (anti)neutrino interactions. However, all of these improvements are voided without a control of the configuration, chemical composition, size, and mass of the neutrino targets comparable to the one traditionally achieved in electron scattering experiments. Furthermore, available measurements of various (anti)neutrino exclusive processes and cross-sections on nuclei indicate many outstanding discrepancies among different experiments, as well as with existing theoretical models [3]. The limited resolution and acceptance of some of those measurements, and the complexity of the weak current (compared to the electromagnetic one) and of the associated nuclear effects in heavy nuclei are typically responsible for the observed discrepancies. To this end, in addition to a high experimental resolution, a large acceptance, and a complete control of the targets, a necessary condition for any program of precision measurements with (anti)neutrino interactions is to have a complementary control target free from nuclear effects: hydrogen (free proton) ¹.

The only available data from $\nu(\bar{\nu})$ -H interactions were collected by the early bubble chamber experiments ANL [4], BNL [5], BEBC [6, 7], and FNAL [8, 9]. In spite of the excellent experimental resolution of those measurements, the overall statistics is limited to about 16,000 events and is insufficient for current needs. Since then safety requirements related to the underground operation and practical considerations favoring modern electronic detectors have prevented new experimental measurements of high statistics $\nu(\bar{\nu})$ -H samples.

In this paper we propose a novel approach for precision measurements of $\nu(\bar{\nu})$ -H Charged Current (CC) interactions, which is both simple and safe to implement. Interactions on hydrogen are extracted by subtracting measurements on a dedicated graphite (pure C) target from those on a dedicated CH₂ plastic target, within a low-density high resolution detector. This concept appears to be a viable and realistic alternative to the use of liquid H₂ detectors to obtain high statistics samples of (anti)neutrino interactions on hydrogen.

This paper is organized as follows. In Sec. II we discuss how we can achieve a control of (anti)neutrino targets comparable to electron scattering experiments, as well as the basic concept of the subtraction between CH₂ and C targets. In Sec. III we present a detailed kinematic selection of $\nu(\bar{\nu})$ -H interactions from the CH₂ plastic target for various event topologies. In Sec. IV we discuss our results and in Sec. V we summarize our findings.

¹ Elastic scattering off electrons (mainly NC) can also provide complementary information free from nuclear effects. However, the limited statistics and the additional smearing associated to the outgoing neutrino and the beam divergence limit the physics sensitivity of this channel.

II. CONTROL OF NEUTRINO TARGETS

All detectors for neutrino interactions suffer from a tension between the opposing requirements of a large target mass versus the detector resolution necessary to achieve the physics goals. Furthermore, in most fine-grained neutrino detectors the active detector, consisting of several different materials and components, also provides the target mass. A drawback of this configuration is the difficulty to precisely control the target chemical composition and mass, limiting the ultimate precision achievable in the measurements.

A detector technology designed to offer a solution to the outstanding issues above is a Straw Tube Tracker (STT) in which the neutrino targets are physically separated from the actual tracking system (of negligible mass). To achieve high resolution measurements, the target mass is spread out uniformly throughout the entire tracking volume, by keeping the average density low enough – similar to that of liquid deuterium $\rho \sim 0.17 \text{ g/cm}^3$ – to have a detector transparent (size comparable to one radiation length) to final state particles produced in neutrino interactions. This detector concept is rather flexible and its main operating parameters can be adapted to different detector configurations and geometries. Examples of different implementations of the STT technology can be found in the CDR of the DUNE experiment [2] and in a recently proposed near detector enhancement for the Long-Baseline Neutrino Facility (LBNF) [10].

The detector considered here is based upon a central STT inserted in a 0.6 T magnetic field and surrounded by a 4π electromagnetic calorimeter (ECAL) [11]. The base tracking technology is provided by low-mass straws similar to the ones used in many modern experiments for precision physics or the search for rare processes [12–16]. Thin layers – typically 1-2% of radiation length – of various target materials (100% chemical purity) are alternated with straw layers so that they represent more than 95% of the total detector mass (the mass of the straws being $< 5\%$). This feature, combined with the excellent vertex, angular, momentum, and timing resolutions are key factors to correctly associate neutrino interactions to each target material, as well as for an accurate measurement of the four-momenta of the final state particles. As a result, we can achieve a control of the configuration, chemical composition, size, and mass of the (anti)neutrino targets comparable to electron scattering experiments.

In this paper we will focus on two specific materials to be used as (anti)neutrino targets within the detector described above: polypropylene (CH_2) and graphite (pure C). The former is one of the plastic materials with the highest hydrogen content and can be easily manufactured in thin foils of arbitrary size. Both targets have comparable thickness in terms of radiation length and are alternated throughout the entire tracking volume to ensure that they result in the same detector acceptances for final state particles. We further assume that they are exposed simultaneously to the same (anti)neutrino beam. By performing a statistical subtraction between the data collected from the CH_2 plastic and the ones collected from the graphite, we can in principle obtain (anti)neutrino interactions on a hydrogen target, i.e. on free protons. Given the purity (100%) of the CH_2 and C targets and the accuracy in associating the interactions to each target, the normalization of the H signal and the C background is based upon the corresponding relative abundances in CH_2 . This technique can be safely implemented and can offer a relatively large (~ 0.7 ton with 5 tons of CH_2) target mass of hydrogen. The main issues to address are the physics sensitivity achievable and whether the uncertainties associated to the subtraction procedure allow competitive $\nu(\bar{\nu})$ -H measurements. In the following we will present detailed studies of the corresponding event

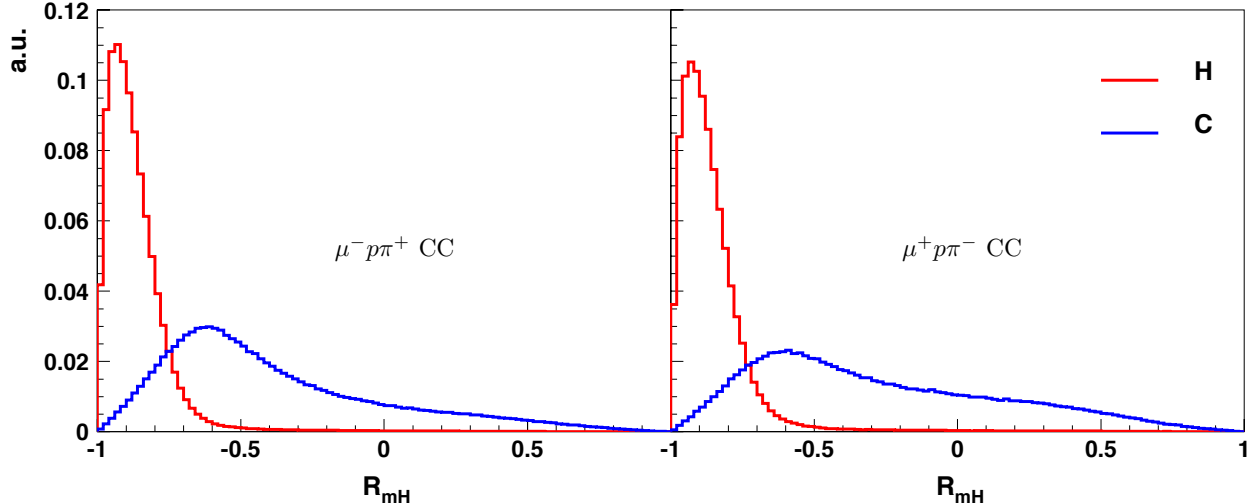


FIG. 1. Comparison of the reconstructed p_T asymmetry $R_{mH} = (p_T^m - p_T^H)/(p_T^m + p_T^H)$ in $\nu_\mu p \rightarrow \mu^- p \pi^+$ and $\bar{\nu}_\mu p \rightarrow \mu^+ p \pi^-$ processes on H (signal) and in the corresponding background topologies from the C nucleus. Results for both neutrino (left panel) and antineutrino (right panel) interactions are shown. All distributions are normalized to unit area.

selection with realistic assumptions for the detector smearing and the physics modeling.

III. SELECTION OF $\nu(\bar{\nu})$ -H INTERACTIONS

The detection technique described in Sec. II allows a complete control of the (anti)neutrino targets in both size and material(s), as well as an accurate location of the interaction vertices within each target element. However, the H content by weight in the CH_2 target is only 14.4% of the total and most of the interactions are still originated from the C nucleus.

We can improve the signal/background ratio in the selection of H interactions by exploiting the event kinematics. Since the H target is at rest, CC events are expected to be perfectly balanced in a plane transverse to the beam direction (up to the tiny beam divergence) and the muon and hadron vectors are back-to-back in the same plane. Instead, events from nuclear targets are affected by the smearing with the energy-momentum distribution of bound nucleons (Fermi motion and binding), the off-shell modifications of bound nucleons, meson exchange currents and nuclear shadowing [3, 17–19], as well as by final state interactions (FSI) [3]. These nuclear effects result in a significant missing transverse momentum and a smearing of the transverse plane kinematics. The use of transverse plane variables and event kinematics to select various Neutral Current (NC) and CC (anti)neutrino topologies was pioneered by the NOMAD experiment [20]. The analysis described in this paper is largely based upon the variables and techniques developed and validated with NOMAD data [21–23].

A. Analysis framework

We simulate (anti)neutrino interactions on CH_2 , H, and C targets with three different event generators: NuWro [24], GiBUU [25], and GENIE [26]. While we use NuWro as our default

generator, we compare our results with both GiBUU and GENIE to check the sensitivity of our analysis to the details of the input modeling. These generators are based upon different assumptions and modeling of nuclear effects and final state interactions, with GiBUU using a conceptually different approach from heavy ion physics, based upon the Boltzmann-Uehling-Uhlenbeck equation for the particle propagation through the nuclear medium. For a detailed review and comparison of the generators used we refer to Ref. [27]. The studies of nuclear FSI by the MINER ν A and T2K experiments [28, 29] have found an unphysical excess of hA elastic scattering processes in the FSI simulated by GENIE, which is in disagreement with (anti)neutrino data. We follow the corresponding prescriptions by MINER ν A and T2K and discard such elastic hA FSI processes in GENIE. We generate inclusive CC interactions including all processes available in the event generators – quasi-elastic (QE), $\Delta(1232)$ and higher resonances (RES), non-resonant processes and deep inelastic scattering (DIS) – with defaults settings and the input (anti)neutrino spectra expected in the Long-Baseline Neutrino Facility (LBNF) [10, 30].

We use the GEANT4 [31] program to evaluate detector effects and apply to all final state particles a parameterized reconstruction smearing consistent with the NOMAD data [20]. The detector smearing has also been independently checked with the FLUKA [32] simulation program in Ref. [10]. The acceptance for individual final state particles ($p, n, \pi^\pm, \pi^0, \mu$) takes into account the detector geometry, the event topology, and the material traversed by the particles and is folded into the analysis. We emphasize that the STT detector has been explicitly designed to offer the same acceptance for particles produced in both the CH₂ and graphite targets, as discussed in Sec. II. On average, the momentum resolution is about 5% and the angular resolution is about 2 mrad for charged tracks. The reconstruction of protons is typically worse due to the shorter track length, with average momentum resolution of 6.5% for H events and 8.4% for C events. The difference between H and C events is related to the different momentum and angular distributions introduced by nuclear effects. The vertex resolution can vary from 100 μm to about 500 μm for multi-track events, depending upon the geometry and the event topology [20]. We note that this parameter is not critical in STT – even for single track events (Sec. III B 2) – since the actual targets have 100% chemical purity and represent more than 95% of the total detector mass (Sec. II). Particle identification is provided by various methods including dE/dx , range, and transition radiation in STT, as well as the energy deposition, timing and track segments in the surrounding ECAL and muon identifier. For more details about the detector performance we refer to Refs. [2, 10, 20].

We analyze ν_μ and $\bar{\nu}_\mu$ CC interactions originated from the CH₂ and graphite targets described in Sec. II. We determine the momentum vectors of charged particles from the track curvature in the B filed, while for neutral particles we use either the energy deposited in the various sub-detectors or, whenever available, the secondary charged tracks originated by the neutral particles in STT. The momentum vector of the total hadron system, \vec{p}_H , is obtained from the sum of the momenta of all the reconstructed final state hadrons [21].

In the following section we discuss a unified approach to the kinematic selection of all the event topologies available in ν_μ -H and $\bar{\nu}_\mu$ -H CC interactions, as well as the corresponding inclusive samples. For more details about the analysis technique used we refer to Ref. [21].

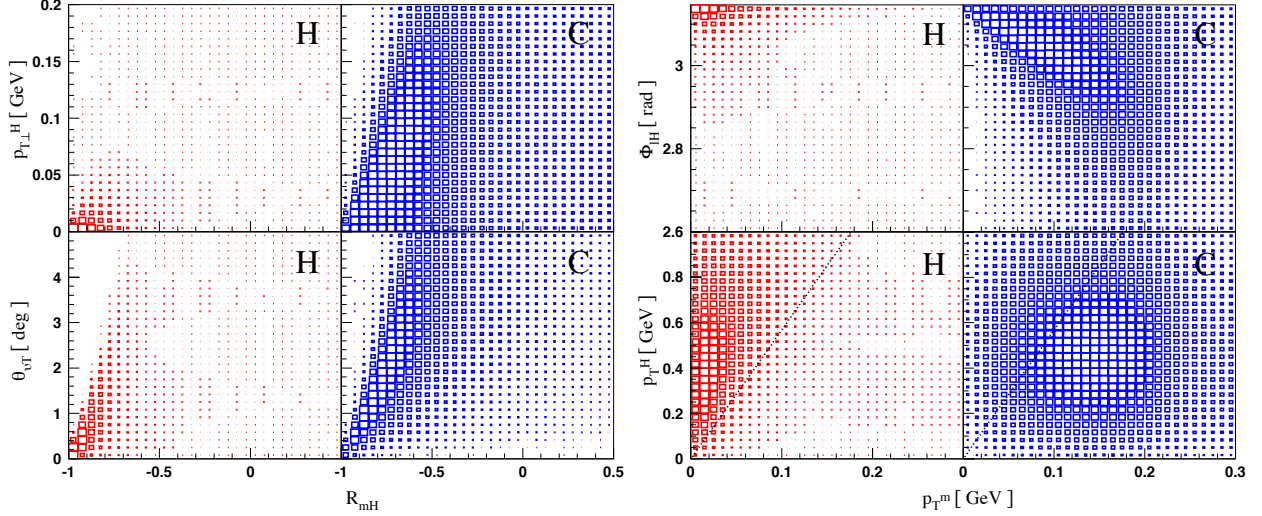


FIG. 2. Some of the correlations between kinematic variables used to construct $\ln \lambda^H$ and $\ln \lambda_4^H$ for H signal (red color) and C background (blue color) exclusive $\mu^- p \pi^+$ CC topologies. The dotted line on the bottom right plots corresponds to a cut $R_{mH} < -0.7$ (Fig. 1).

B. Kinematic analysis

1. Selection of $\nu_\mu p \rightarrow \mu^- p \pi^+$ and $\bar{\nu}_\mu p \rightarrow \mu^+ p \pi^-$

In order to illustrate the potential of the technique we propose for the measurement of H interactions, we start from an analysis based upon simple kinematic cuts and the cleanest topologies $\nu_\mu p \rightarrow \mu^- p \pi^+$ and $\bar{\nu}_\mu p \rightarrow \mu^+ p \pi^-$, mainly originated from resonance production. Detailed GEANT4 simulations indicate that the average proton reconstruction efficiency² is about 93% for H events and 67% in C events, since in this latter case nuclear effects result, on average, in smaller kinetic energies and larger angles for the protons. As discussed in Sec. III A, the final state particles from these processes on H can be accurately reconstructed in the detector described in Sec. II, thus resulting in an excellent measurement of all the relevant kinematic variables.

The most powerful kinematic variable to separate H interactions from the ones originated in nuclear targets is $R_{mH} \equiv (p_T^m - p_T^H)/(p_T^m + p_T^H)$, the asymmetry between the missing transverse momentum, p_T^m , and the transverse momentum of the hadron vector, p_T^H . For H interactions p_T^m is consistent with zero up to reconstruction effects and hence we expect $R_{mH} \sim -1$. Instead, if the interactions occur inside a nuclear target we expect, on average, a substantial p_T^m together with smaller values of p_T^H , due to the nuclear smearing. Furthermore, the missing transverse momentum is mainly generated inside the hadron system and it is expected to be correlated with the latter. All these nuclear effects result in much larger values of R_{mH} . As shown in Fig. 1, this variable can be efficiently used to separate H interactions, as well as to probe various aspects of the nuclear smearing. Another useful variable is the magnitude of the component of the hadron transverse momentum perpendicular to the

² To be reconstructed the proton track must have enough hits to allow a momentum determination from the bending in B field. In principle some of the events failing this requirement can still be reconstructed from the energy deposition in the available hits. We do not make any attempt to recover such protons.

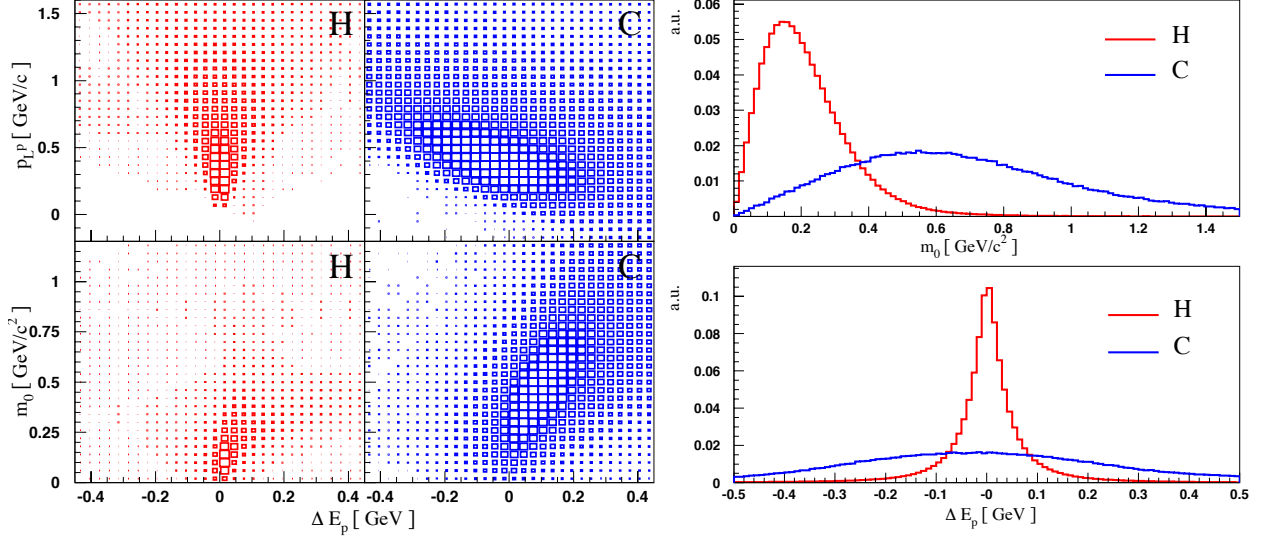


FIG. 3. Some of the kinematic variables and correlations used to construct $\ln \lambda_{\text{IN}}^H$ for H signal (red color) and C background (blue color) exclusive $\mu^- p \pi^+$ CC topologies. All histograms in the right plots are normalized to unit area.

transverse momentum of the lepton, $p_{T\perp}^H$. In H interactions the transverse momenta of the lepton and of the hadron system are back-to-back, thus resulting in a sharp peak around zero in $p_{T\perp}^H$. Interactions from nuclear targets have a much broader distribution originating from the nuclear smearing. The use of this variable to study H interactions within composite targets was suggested in Ref. [33]. Since $p_{T\perp}^H$ is selecting topologies in which the transverse momenta of the lepton and the hadron system are back-to-back, the effect of this variable is similar to the use of the angle between those transverse vectors, Φ_{lH} . Used as a single variable in the H selection, $p_{T\perp}^H$ has less discriminating power than both R_{mH} and the other kinematic variables discussed in this section. However, it provides information complementary to R_{mH} , so that the combined effect of both these variables improves the overall selection efficiency.

The use of simple cuts $R_{mH} < -0.6$ and $p_{T\perp}^H < 0.03$ GeV/c provides a selection of $\nu_\mu p \rightarrow \mu^- p \pi^+$ H interactions from the CH₂ plastic with an efficiency of 93% and a purity of 86%, including non-resonant backgrounds as well as higher order resonances above $\Delta(1232)$. Similarly, we can select the $\bar{\nu}_\mu p \rightarrow \mu^+ p \pi^-$ topology with a 89% efficiency and a 84% purity.

We can improve the selection of H interactions by using multivariate techniques exploiting the complete event kinematics [21–23]. Assuming the two momentum vectors of the lepton and hadron system, we have in total 3 transverse and 2 longitudinal degrees of freedom in the event selection, due to the invariance for an arbitrary rotation in the transverse plane. Since we want to separate the same CC events with and without nuclear effects, we can further assume that the overall reconstructed energy spectra are similar, thus somewhat reducing the rejection power of one of the longitudinal variables compared to the transverse ones. As a result, we can define a complete kinematic set as 3 transverse plus one longitudinal variables. We select the angle between the total visible momentum vector and the incident neutrino direction (z axis), $\theta_{\nu T}$, as the variable including longitudinal information. This variable is expected to be close to zero in H interactions, up to the tiny beam divergence, while it is much larger in interactions originated from nuclear targets.

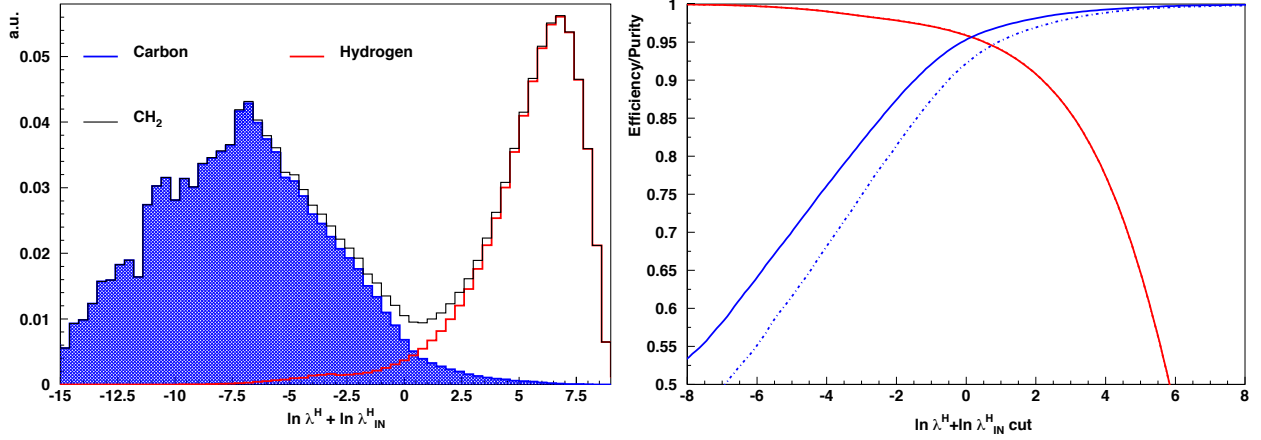


FIG. 4. Left plot: Distributions of $\ln \lambda^H + \ln \lambda_{\text{IN}}^H$ for the H signal, the C background, and the CH_2 plastic (sum) for the exclusive $\mu^- p \pi^+$ CC topologies. The multiple peaks are the effect of the binning used to build \mathcal{L}^H and $\mathcal{L}_{\text{IN}}^H$. The C distribution is normalized to unit area while the H distribution is normalized to the expected relative abundance in CH_2 . Right plot: Efficiency (red color) and purity (blue color) as a function of the cut on $\ln \lambda^H + \ln \lambda_{\text{IN}}^H$ for the kinematic selection of the exclusive processes $\nu_\mu p \rightarrow \mu^- p \pi^+$ (solid lines) and $\bar{\nu}_\mu p \rightarrow \mu^+ p \pi^-$ (dashed-dotted lines) on hydrogen from the CH_2 target.

We use likelihood functions incorporating multi-dimensional correlations among kinematic variables. A study of the kinematic selection suggests the following function using only three-dimensional correlations:

$$\mathcal{L}^H \equiv [[R_{mH}, p_{T\perp}^H, \theta_{\nu T}], p_T^m, \Phi_{lH}] \quad (1)$$

where the square brackets denote correlations (Fig. 2). The \mathcal{L}^H function is over-constrained in the transverse plane to compensate for the reduced phase space. An optimal function strictly based upon a complete set of kinematic variables is the four-dimensional:

$$\mathcal{L}_4^H = [p_T^H, p_T^m, \Phi_{lH}, \theta_{\nu T}] \quad (2)$$

which incorporates the R_{mH} variable through its underlying correlation $[p_T^H, p_T^m]$ (Fig. 2). Although the use of the \mathcal{L}_4^H function requires a larger statistics to achieve a sensible binning, we used it for our kinematic selection and obtained results similar to \mathcal{L}^H . We build the \mathcal{L}^H and \mathcal{L}_4^H probability density functions (pdf) for the two test hypotheses of H interactions (signal) and C interactions (background). The individual pdf are properly smoothed and are built with samples independent from the test ones to avoid large statistical biases. As it is common practice, the logarithm of the final likelihood ratio between signal and background hypotheses, $\ln \lambda^H$ or $\ln \lambda_4^H$, is used as discriminant [21].

We can also exploit the information related to the individual particles inside the hadron system. For $\mu^\mp p \pi^\pm$ topologies we have a total of 3 additional degrees of freedom, since the total hadron momentum vector is constrained by the global event kinematics in \mathcal{L}^H and \mathcal{L}_4^H . We select one of such variables as the difference ΔE between the energy of the neutrino calculated from the μ and π momenta by applying energy-momentum conservation and the

| Process | ν_{μ} -H CC | | | | $\bar{\nu}_{\mu}$ -H CC | | | | | |
|--------------------|-------------------|-------------------|-------------------------|-----------|-------------------------|-----------------|-----------|-------------------|---------------------|-----------|
| | $\mu^- p \pi^+$ | $\mu^- p \pi^+ X$ | $\mu^- n \pi^+ \pi^+ X$ | Inclusive | $\mu^+ p \pi^-$ | $\mu^+ n \pi^0$ | $\mu^+ n$ | $\mu^+ p \pi^- X$ | $\mu^+ n \pi \pi X$ | Inclusive |
| Eff. ε | 96% | 89% | 75% | 93% | 94% | 84% | 75% | 85% | 82% | 80% |
| Purity | 95% | 93% | 70% | 93% | 95% | 84% | 80% | 94% | 84% | 84% |

TABLE I. Efficiency ε and purity for the kinematic selection of H interactions from the CH₂ plastic target using the likelihood ratio $\ln \lambda^{\text{H}} + \ln \lambda_{\text{IN}}^{\text{H}}$ or $\ln \lambda_4^{\text{H}} + \ln \lambda_{\text{IN}}^{\text{H}}$. For the $\mu^+ n$ QE topologies $\ln \lambda_{\text{QE}}^{\text{H}}$ is used instead. The cuts applied for each channel are chosen to maximize the sensitivity defined as $S/\sqrt{S+B}$, where S is the H signal and B the C background. The CC inclusive samples are obtained from the combination of the corresponding exclusive channels.

one reconstructed from the sum of the momentum vector of all 3 particles $\mu^{\mp} p \pi^{\pm}$:

$$\Delta E_p = \frac{m_{\mu}^2 - m_{\pi^{\pm}}^2 + 2M_p(E_{\mu} + E_{\pi^{\pm}}) - 2p_{\mu} \cdot p_{\pi^{\pm}}}{2(M_p - E_{\mu} - E_{\pi^{\pm}} + |\vec{p}_{\mu}| \cos \theta_{\mu} + |\vec{p}_{\pi^{\pm}}| \cos \theta_{\pi^{\pm}})} - |\vec{p}_{\mu} + \vec{p}_{\pi^{\pm}} + \vec{p}_p| \quad (3)$$

where $M_p, M_n, m_{\mu}, m_{\pi^{\pm}}$ are the masses of the proton, neutron, muon, and pion, respectively, $p_{\mu}(\pi^{\pm}), \vec{p}_{\mu}(\pi^{\pm}), E_{\mu}(\pi^{\pm})$ and $\theta_{\mu}(\pi^{\pm})$ are the 4-momentum, momentum vector, energy and angle of the outgoing muon (pion), and \vec{p}_p is the proton momentum vector. The variable ΔE is close to zero up to reconstruction effects in hydrogen, while it is significantly larger in carbon events, due to the nuclear smearing. Another useful variable is the invariant mass of the reconstructed neutrino, calculated as $m_0 = |p_{\mu} + p_{\pi^{\pm}} + p_p - p_N|$ where p_p and p_N are the 4-momenta of the outgoing proton and of the target proton assumed at rest, respectively. We use the following likelihood function using information from the internal $p\pi$ structure:

$$\mathcal{L}_{\text{IN}}^{\text{H}} = [\Delta E_p, p_L^p, m_0] \quad (4)$$

where p_L^p is the longitudinal component of the proton momentum vector along the beam direction. Figure 3 shows the main variables and correlations included in $\mathcal{L}_{\text{IN}}^{\text{H}}$. Since $\mathcal{L}_{\text{IN}}^{\text{H}}$ is essentially independent from \mathcal{L}^{H} and \mathcal{L}_4^{H} we multiply the corresponding density functions and use the sum $\ln \lambda^{\text{H}} + \ln \lambda_{\text{IN}}^{\text{H}}$ or $\ln \lambda_4^{\text{H}} + \ln \lambda_{\text{IN}}^{\text{H}}$ as the final discriminant for our analysis.

The distributions of $\ln \lambda^{\text{H}} + \ln \lambda_{\text{IN}}^{\text{H}}$ for the H signal and the C background in $\mu^- p \pi^+$ topologies are shown in Fig. 4 (left plot). The corresponding purity and efficiency achievable as a function of the $\ln \lambda^{\text{H}} + \ln \lambda_{\text{IN}}^{\text{H}}$ cut are given in the right plot of Fig. 4, for both the $\nu_{\mu} p \rightarrow \mu^- p \pi^+$ and $\bar{\nu}_{\mu} p \rightarrow \mu^+ p \pi^-$ samples. Both the efficiency and the purity appear relatively uniform as a function of the neutrino energy. Table I summarizes the results obtained by applying the cut on $\ln \lambda^{\text{H}} + \ln \lambda_{\text{IN}}^{\text{H}}$ maximizing the sensitivity $S/\sqrt{S+B}$, where S is the H signal and B the C background. The fact that the maximum sensitivity corresponds to regions with high purity for the selected H signal indicates that the kinematic selection is optimal.

The use of a multi-variate selection further reduces the background levels with respect to the simple cut analysis, without dramatically changing the overall results. A key advantage of this approach is that the likelihood function allows to assign, on an event-by-event basis, the probability that a given (anti)neutrino interaction originated from either the hydrogen or the carbon nucleus. Furthermore, it provides a better control of the selection procedure by easily varying the efficiency/purity and by offering relatively clean control samples.

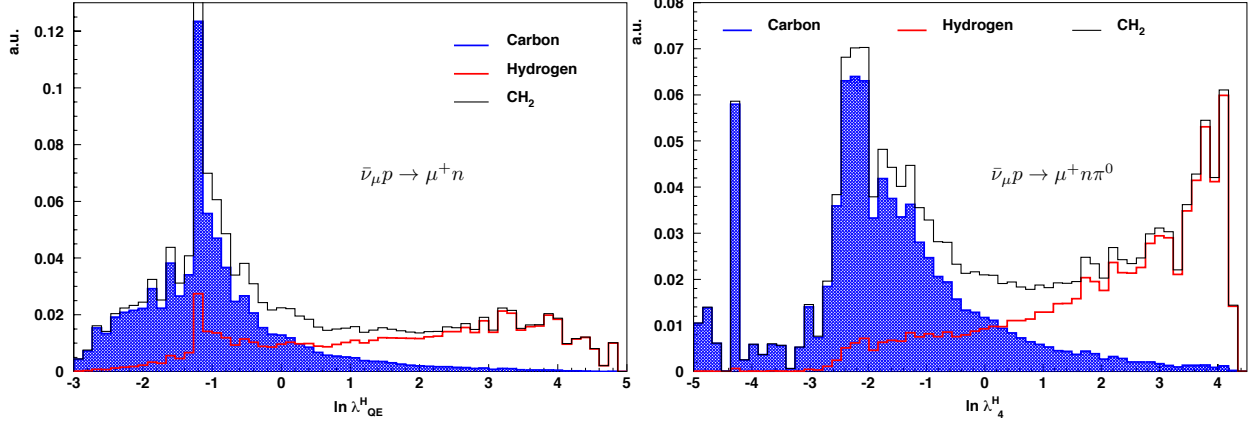


FIG. 5. Left plot: Distributions of $\ln \lambda_{QE}^H$ for the H signal, the C background, and the CH₂ plastic (sum) for the selection of $\bar{\nu}_\mu p \rightarrow \mu^+ n$ QE events. Right plot: Distributions of $\ln \lambda_4^H$ for the selection of $\bar{\nu}_\mu p \rightarrow \mu^+ n \pi^0$ events. The multiple peaks are the effect of the binning used to build the likelihood functions. The C distributions are normalized to unit area while the H distributions are normalized to the expected relative abundance in CH₂. See the text for details.

2. Selection of $\bar{\nu}_\mu p \rightarrow \mu^+ n$ QE

An important exclusive process available in $\bar{\nu}_\mu$ CC interactions is the quasi-elastic $\bar{\nu}_\mu p \rightarrow \mu^+ n$ on hydrogen. The reconstruction of this topology is more complex because of the presence of a neutron in the final state and a single charged track. We performed detailed GEANT4 simulations of the detector to study the reconstruction efficiency of the neutrons. The results were independently checked using FLUKA simulations. About 25% of the neutrons produced in $\bar{\nu}_\mu p \rightarrow \mu^+ n$ QE events on H interact inside the STT and can be detected. An additional fraction of about 55% of the neutrons can be detected in the ECAL [11] surrounding the tracker, thus allowing a combined reconstruction efficiency around 80%. Conversely, the combined detection efficiency for neutrons originated from the C background events is only about 65%, since they are typically affected/produced by nuclear effects, resulting, on average, in a smaller kinetic energy. For events with a single charged track the resolution on the position of the primary vertex is worse than for multi-track events, and is essentially defined by the thickness of a single CH₂ (or C) target plane by noting the absence of straw tube hits preceding the presumed target. However, events can still be efficiency associated to the correct target material, due to the lightness of the tracking straws and the purity of the target itself. The corresponding uncertainty is given by the ratio between the thickness of the straw walls and the thickness of a single CH₂ target, resulting in an efficiency > 99%. From the positions of the primary vertex and that of the neutron interaction within the detector we can reconstruct the neutron line of flight. Assuming that the target proton is at rest, we calculate the energy of the incoming antineutrino as:

$$E_\nu = \frac{M_n^2 - m_\mu^2 + 2M_p E_\mu - M_p^2}{2(M_p - E_\mu + |\vec{p}_\mu| \cos \theta_\mu)} \quad (5)$$

with the same notations as in Eq.(3). The energy of the neutron is $E_n = E_\nu + M_p - E_\mu$ and the momentum vector of the neutron is obtained from the measured neutron direction

and the calculated energy E_n ³. We note that Eq.(5) is correct only for interactions on hydrogen and not for the ones on carbon, due to nuclear effects. We use a realistic smearing on the measured direction of the neutron obtained from a detailed FLUKA simulation of the detector and including the non gaussian tails, mainly related to elastic scattering of the neutrons before interacting. We can then reconstruct the complete event kinematics for $\bar{\nu}_\mu p \rightarrow \mu^+ n$ interactions on hydrogen and apply the same kinematic selection described in Sec. III B. The resolution achievable on many of the kinematic variables is dominated by the reconstruction of the neutron direction rather than that of the μ^+ momentum vector, given the excellent momentum and angular resolution of the STT.

An additional background source to consider for the selection of the process $\bar{\nu}_\mu p \rightarrow \mu^+ n$ on H is given by the uncorrelated neutrons originated from (anti)neutrino interactions occurring in the large amount of materials surrounding the STT, including the ECAL, the magnet elements, and the external rocks. We estimate this background by randomly overlaying a genuine $\bar{\nu}_\mu p \rightarrow \mu^+ n$ event on H with a neutron extracted from either a different CH₂ event or from an event in the surrounding materials. We then reconstruct the event kinematics using the measured direction of the random neutron and the calculated energy E_n , as described above. Since the random neutron is uncorrelated with the primary vertex from the $\bar{\nu}_\mu p \rightarrow \mu^+ n$ interaction on H, the resulting kinematic distributions are inconsistent with those expected from a genuine H signal. In addition, we can require that the measured time difference between the interaction point of the random neutron and the primary vertex is consistent with the expected time of flight.

We have less kinematic information available for the selection of $\bar{\nu}_\mu p \rightarrow \mu^+ n$ QE on H with respect to other channels. We use the optimal function \mathcal{L}_4^H from Eq.(2) as the basis of our kinematic analysis. The likelihood function $\mathcal{L}_{\text{IN}}^H$, as defined in Eq.(4), is not strictly applicable, since the hadron system is composed of a single neutron without internal structure. However, we can still exploit one additional longitudinal degree of freedom with respect to Eq.(4). In analogy of Eq.(3), we calculate $\Delta E_n = E_\nu - |\vec{p}_\mu + \vec{p}_n|$, where E_ν is given by Eq.(5) and \vec{p}_n is the neutron momentum calculated as described above. We use the following likelihood function for the selection of $\bar{\nu}_\mu p \rightarrow \mu^+ n$ QE on H:

$$\mathcal{L}_{\text{QE}}^H = [[p_T^H, p_T^m, \Phi_{lH}, \theta_{\nu T}], \Delta E_n, p_L^n] \quad (6)$$

which is over-constrained to compensate for the reduced phase space. The variable p_L^n represents the longitudinal component of the neutron momentum vector along the beam direction. We note that, although the two-dimensional correlation $[\Delta E_n, p_L^n]$ appears similar to the corresponding one in Eq.(4), it has a different role in the QE channel, as a part of the global event kinematics. We therefore include it into a single likelihood function, since it is expected to be correlated with the other kinematic variables. Figure 5 shows the distributions of $\ln \lambda_{\text{QE}}^H$ for the H signal and the C background. Table I summarizes the efficiency and purity for a cut on $\ln \lambda_{\text{QE}}^H$ maximizing the sensitivity of the analysis.

3. Selection of $\bar{\nu}_\mu p \rightarrow \mu^+ n \pi^0$

Another exclusive process available only in $\bar{\nu}_\mu$ CC interactions is $\bar{\nu}_\mu p \rightarrow \mu^+ n \pi^0$ on hydrogen, mainly originated from resonance production. The kinematic selection of this channel is

³ It is possible to calculate the complete momentum vector of the neutron from energy-momentum conservation. However, the direct use of transverse plane kinematics would void the kinematic selection against the C background. For this reason we combine the calculated energy E_n with the measured neutron direction.

similar to the one discussed in Sec. III B 1 for the complementary process $\bar{\nu}_\mu p \rightarrow \mu^+ p \pi^-$, with the exception of a few specific features related to the reconstruction of the neutron and the π^0 . The relative fractions of these two channels are about comparable in $\bar{\nu}_\mu$ CC interactions on hydrogen.

For the reconstruction of the π^0 we distinguish the case in which γ s are converted into e^+e^- pairs within the STT volume and the one in which γ s are detected only in the surrounding ECAL. In the former case we use the momentum and angle smearing for e^\pm tracks in STT, while in the latter case we apply the corresponding smearing obtained from a detailed ECAL simulation. On average, about 50% of all π^0 have at least one converted γ within the STT volume, providing a more accurate reconstruction of the π^0 direction. We calculate the energy of the neutrons interacting in the detector as:

$$E_n = \frac{M_n^2 - m_\mu^2 - m_{\pi^0}^2 + 2M_p(E_\mu + E_{\pi^0}) - 2\vec{p}_\mu \cdot \vec{p}_{\pi^0} - M_p^2}{2(M_p - E_\mu - E_{\pi^0} + |\vec{p}_\mu| \cos \theta_\mu + |\vec{p}_{\pi^0}| \cos \theta_{\pi^0})} + M_p - E_\mu - E_{\pi^0} \quad (7)$$

where $p_{\pi^0}, \vec{p}_{\pi^0}, E_{\pi^0}$ and θ_{π^0} are the 4-momentum, momentum vector, energy and angle of the outgoing π^0 , respectively. The first term on the r.h.s. of Eq.(7) represents the neutrino energy calculated from the muon and π^0 momenta using energy-momentum conservation. We note that Eq.(7) is correct only for interactions on hydrogen since it assumes a target proton at rest. We reconstruct the neutron momentum vector \vec{p}_n following the same procedure described in Sec. III B 2 for the QE process, combining the measured (smeared) direction of the neutron with the energy E_n calculated from Eq.(7).

We use the likelihood function \mathcal{L}_4^H from Eq.(2) to describe the global event kinematics. In analogy to the $\bar{\nu}_\mu p \rightarrow \mu^+ p \pi^-$ case, it is possible to exploit the additional information related to the individual particles within the hadron system with the function $\mathcal{L}_{\text{IN}}^H = [\Delta E_{\pi^0}, p_L^{\pi^0}, m_0]$, where $\Delta E_{\pi^0} = E_\nu - | \vec{p}_\mu + \vec{p}_{\pi^0} + \vec{p}_n |$, E_ν is the neutrino energy calculated from the muon and neutron momenta using energy-momentum conservation, and $p_L^{\pi^0}$ is the longitudinal component of the momentum vector of the π^0 . The use of ΔE_{π^0} is preferable with respect to the equivalent quantity for the neutron, ΔE_n , since this latter is partially biased by the calculation of the neutron energy from Eq.(7). Since the average reconstruction smearing for the neutron and π^0 is larger than for most charged particles, the $\ln \lambda_{\text{IN}}^H$ improves only marginally the selection of $\bar{\nu}_\mu p \rightarrow \mu^+ n \pi^0$ on H and can be dropped for this channel. Figure 5 shows the distributions of $\ln \lambda_4^H$ for the H signal and the C background. Table I summarizes the efficiency and purity for a cut on $\ln \lambda_4^H$ maximizing the sensitivity of the analysis. Similar results are obtained with $\ln \lambda^H$.

4. Selection of $\nu_\mu p \rightarrow \mu^- p \pi^+ X$ and $\bar{\nu}_\mu p \rightarrow \mu^+ p \pi^- X$

In this section and in the following one we consider the collective selection of all the inelastic topologies produced in $\nu_\mu p$ and $\bar{\nu}_\mu p$ CC interactions on H and different from the $\mu^- p \pi^+$, $\mu^+ p \pi^-$, and $\mu^+ n \pi^0$ topologies discussed in Sec. III B 1 and Sec. III B 3. These samples are dominated by the Deep Inelastic Scattering (DIS): about 63% of the $\mu^- \pi^+ X$ events and 7% of the $\mu^- p \pi^+$ sample have $W > 1.8$ GeV with the default low energy beam option considered.

The inelastic $\nu_\mu p \rightarrow \mu^- \pi^+ X$ and $\bar{\nu}_\mu p \rightarrow \mu^+ \pi^- X$ samples on H are characterized, in general, by a higher multiplicity and a worse reconstruction of some of the events, compared to the $\mu^- p \pi^+$, $\mu^+ p \pi^-$, and $\mu^+ n \pi^0$ topologies. The larger detector smearing directly affects

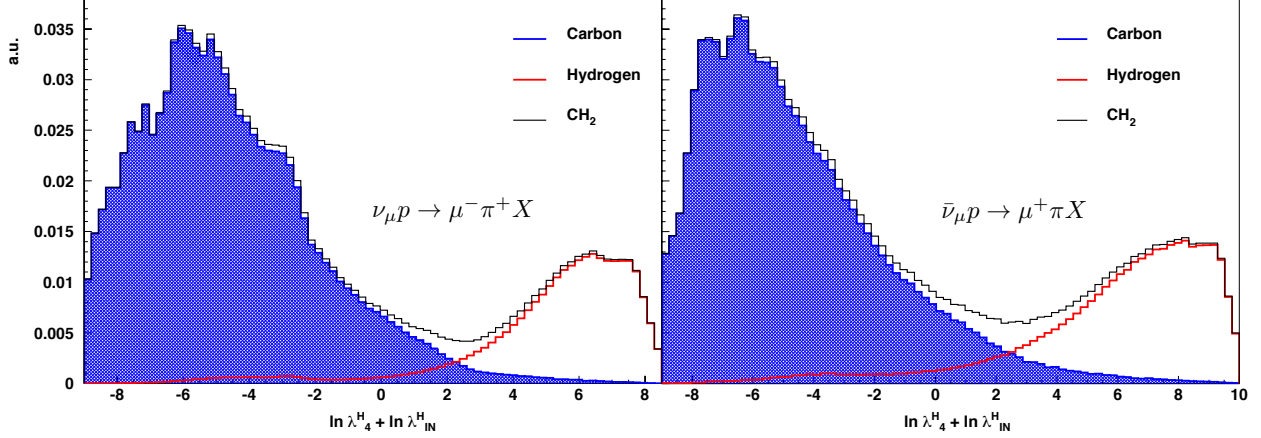


FIG. 6. Distributions of $\ln \lambda_4^H + \ln \lambda_{\text{IN}}^H$ for the H signal, the C background, and the CH_2 plastic (sum) for $\nu_\mu p \rightarrow \mu^- \pi^+ X$ (left plot) and $\bar{\nu}_\mu p \rightarrow \mu^+ \pi^- X$ (right plot), including the sum of the subsamples with a proton and a neutron. The multiple peaks are the effect of the binning used to build \mathcal{L}_4^H and $\mathcal{L}_{\text{IN}}^H$. The C distributions are normalized to unit area while the H distributions are normalized to the expected relative abundance in CH_2 . See the text for details.

the reconstruction of the kinematic variables, thus somewhat reducing their discriminating power. However, these effects are even larger for the DIS interactions originated in nuclear targets, primarily because of the final state interactions. We can therefore still achieve an adequate separation of the interactions on hydrogen from the carbon background, which largely dominates the statistics of the $\mu^- \pi^+ X$ and $\mu^+ \pi^- X$ samples from the CH_2 target.

Since we want to select interactions on protons, we require that the total charge measured at the primary vertex is $C = +1$. This cut rejects a large fraction of the interactions on neutrons in background events and has an efficiency of about 23%(33%) for $\nu_\mu(\bar{\nu}_\mu)$ CC interactions on C. We also require the presence of at least one π^+ in $\nu_\mu p$ and one π^- or $\bar{\nu}_\mu p$ events to select inelastic interactions.

In $\nu_\mu p$ and $\bar{\nu}_\mu p$ CC interactions on H we expect a single nucleon – either a proton or a neutron – in the final state, while for interactions on C nuclear effects including final state interactions can result in higher multiplicities. We perform a separate analysis of the two subsamples with a proton and a neutron. In this section we discuss the selection of the subsamples with a reconstructed proton. Detailed GEANT4 simulations indicate that the average proton reconstruction efficiency is about 96% for H events and 74% in C events.

The kinematic selection of $\nu_\mu p \rightarrow \mu^- p \pi^+ X$ and $\bar{\nu}_\mu p \rightarrow \mu^+ p \pi^- X$ on H can exploit additional degrees of freedom with respect to the $\mu^- p \pi^+$, $\mu^+ p \pi^-$, and $\mu^+ n \pi^0$ topologies, due to the higher number of particles in the hadron system. We use the likelihood function \mathcal{L}_4^H from Eq.(2) to describe the global event kinematics. We then tag the single particle within the hadron system potentially affected by the largest nuclear effects by maximizing the magnitude $|\Delta E_{h_i}|$, defined as:

$$\Delta E_{h_i} = \frac{m_{h_i}^2 - m_\mu^2 - (W')^2 + 2M_p(E_\mu + E_{H'}) - 2p_\mu \cdot p_{H'} - M_p^2}{2(M_p - E_\mu - E_{H'} + |\vec{p}_\mu| \cos \theta_\mu + |\vec{p}_{H'}| \cos \theta_{H'})} - \left| \vec{p}_\mu + \sum_k \vec{p}_{h_k} \right| \quad (8)$$

which is calculated for each hadron particle h_i of mass m_{h_i} and momentum vector \vec{p}_{h_i} . The first term on the r.h.s. of Eq.(8) is similar to the equivalent one in Eq.(7), with the π^0

replaced by a reduced hadron system H' excluding the single particle h_i being considered. The quantity $(W')^2 = E_{H'}^2 - |\vec{p}_{H'}|^2$ is the invariant mass of the reduced hadron system, and $E_{H'} = \sum_{k \neq i} E_{h_k}$ and $\vec{p}_{H'} = \sum_{k \neq i} \vec{p}_{h_k}$ are the corresponding energy and momentum vector. We select the hadron particle maximizing the magnitude $|\Delta E_{h_i}|$ and use the corresponding value $\Delta E_{h_i}^{\max}$ (with sign) and the longitudinal momentum of such a particle, $p_L^{h_i}$, as input for the likelihood function ⁴ based upon information internal to the hadron system:

$$\mathcal{L}_{\text{IN}}^{\text{H}} = [\Delta E_{h_i}^{\max}, p_L^{h_i}, m_0,] \quad (9)$$

where we use similar notations as in Eq.(4). Figure 6 shows the distributions of $\ln \lambda_4^{\text{H}} + \ln \lambda_{\text{IN}}^{\text{H}}$ for the H signal and the C background in $\nu_{\mu}p \rightarrow \mu^{-}\pi^{+}X$ and $\bar{\nu}_{\mu}p \rightarrow \mu^{+}\pi X$ topologies. Table I summarizes the efficiency and purity in the selection of both $\nu_{\mu}p \rightarrow \mu^{-}p\pi^{+}X$ and $\bar{\nu}_{\mu}p \rightarrow \mu^{+}p\pi^{-}X$ processes on H with a cut on $\ln \lambda_4^{\text{H}} + \ln \lambda_{\text{IN}}^{\text{H}}$ maximizing the sensitivity of the analysis. Similar results are obtained with $\ln \lambda^{\text{H}} + \ln \lambda_{\text{IN}}^{\text{H}}$.

5. Selection of $\nu_{\mu}p \rightarrow \mu^{-}n\pi^{+}\pi^{+}X$ and $\bar{\nu}_{\mu}p \rightarrow \mu^{+}n\pi\pi X$

In this section we discuss the selection of the subsamples of the inelastic $\nu_{\mu}p$ and $\bar{\nu}_{\mu}p$ CC interactions on H with a detected neutron in the final state and different from the $\mu^{+}n\pi^0$ topologies (Sec. III B 3). These samples are complementary with respect to the similar ones with a reconstructed proton in the final state described in Sec. III B 4. For $\nu_{\mu}p$ CC on H the presence of a neutron in the final state is tagged by requiring that no proton and two π^{+} are present. These criteria correctly tag the neutron in 99.8% of the cases, including events in which the neutron is not detected. Events with a neutron in $\bar{\nu}_{\mu}p$ CC on H are tagged with an efficiency of 88% by requiring that no proton and a number of pions ($\pi^{-} + \pi^{+} + \pi^0$) ≥ 2 with total charge equal to zero are present in the final state. The analysis follows closely the one described in Sec. III B 4 for the subsamples with a proton, the main difference being the treatment of the neutron. We calculate the neutron energy using energy-momentum conservation and Eq.(7) with the π^0 replaced by a reduced hadron system H' excluding the neutron:

$$E_n = \frac{M_n^2 - m_{\mu}^2 - (W')^2 + 2M_p(E_{\mu} + E_{H'}) - 2p_{\mu} \cdot p_{H'} - M_p^2}{2(M_p - E_{\mu} - E_{H'} + |\vec{p}_{\mu}| \cos \theta_{\mu} + |\vec{p}_{H'}| \cos \theta_{H'})} + M_p - E_{\mu} - E_{H'} \quad (10)$$

where we use the same notations as in Eq.(8) with $h_i \equiv n$. We reconstruct the neutron momentum vector \vec{p}_n following the same procedure described in Sec. III B 2 for the QE process, combining the measured (smeared) direction of the neutron with the energy E_n calculated from Eq.(10). For events with more than one neutron detected the calculation above is not applicable and we ignore the neutrons.

We use \mathcal{L}_4^{H} from Eq.(2) to describe the global event kinematics and $\mathcal{L}_{\text{IN}}^{\text{H}}$ from Eq.(9) for the information related to the individual particles inside the hadron system. Since the angular smearing for the detected neutrons (Sec. III B 2) is typically larger than for other particles, we use the track with the largest angle with respect to the beam direction to calculate $\Delta E_{h_i}^{\max}$ in Eq.(9), rather than explicitly maximizing $|\Delta E_{h_i}|$. Figure 6 shows the distributions of $\ln \lambda_4^{\text{H}} + \ln \lambda_{\text{IN}}^{\text{H}}$ for the H signal and the C background in $\nu_{\mu}p \rightarrow \mu^{-}\pi^{+}X$ and

⁴ In principle the same approach can be used for $\mu^{-}p\pi^{+}$, $\mu^{+}p\pi^{-}$, and $\mu^{+}n\pi^0$ topologies, further improving the selection of these channels with respect to the results presented in Sec. III B 1 and Tab. I.

| Process | ν_μ -H CC, $\varepsilon \equiv 75\%$ | | | | $\bar{\nu}_\mu$ -H CC, $\varepsilon \equiv 75\%$ | | | | | |
|---------|--------------------------------------------|-------------------|-------------------------|-----------|--------------------------------------------------|-----------------|-----------|-------------------|---------------------|-----------|
| | $\mu^- p \pi^+$ | $\mu^- p \pi^+ X$ | $\mu^- n \pi^+ \pi^+ X$ | Inclusive | $\mu^+ p \pi^-$ | $\mu^+ n \pi^0$ | $\mu^+ n$ | $\mu^+ p \pi^- X$ | $\mu^+ n \pi \pi X$ | Inclusive |
| Purity | 99% | 99% | 70% | 98% | 99% | 90% | 80% | 98% | 90% | 86% |

TABLE II. Purity achieved with the kinematic selection of H interactions from the CH₂ plastic target using a cut on the likelihood ratio $\ln \lambda^H + \ln \lambda_{\text{IN}}^H$ or $\ln \lambda_4^H + \ln \lambda_{\text{IN}}^H$ resulting in the fixed H signal efficiency ε specified. For the $\mu^+ n$ QE topologies $\ln \lambda_{\text{QE}}^H$ is used instead. For illustration purpose, the value of the efficiency is chosen as the lowest among the ones listed in Tab. I for individual topologies. The CC inclusive samples are obtained from the combination of the corresponding exclusive channels.

$\bar{\nu}_\mu p \rightarrow \mu^+ \pi X$ topologies. Table I summarizes the efficiency and purity in the selection of both $\nu_\mu p \rightarrow \mu^- n \pi^+ \pi^+ X$ and $\bar{\nu}_\mu p \rightarrow \mu^+ n \pi \pi X$ processes on H with a cut on $\ln \lambda_4^H + \ln \lambda_{\text{IN}}^H$ maximizing the sensitivity of the analysis. Similar results are obtained with $\ln \lambda^H + \ln \lambda_{\text{IN}}^H$.

6. Selection of $\nu_\mu p$ and $\bar{\nu}_\mu p$ CC inclusive

In the previous sections we optimized the selection of the various exclusive topologies available in $\nu_\mu p$ and $\bar{\nu}_\mu p$ CC interactions on H by maximizing independently the corresponding sensitivities. The results summarized in Tab. I are characterized by varying efficiencies and purities across different channels. For measurements requiring the inclusive CC samples we can combine the individual exclusive topologies with their corresponding relative fractions in $\nu_\mu p$ and $\bar{\nu}_\mu p$ CC interactions on H. The average efficiency and purity of the resulting inclusive CC samples on H are listed in Tab. I.

An alternative approach to obtain inclusive $\nu_\mu p$ and $\bar{\nu}_\mu p$ CC samples is to tune the kinematic selection to achieve a constant fixed efficiency across all individual channels. We can then directly sum all the selected exclusive topologies independently from the corresponding relative fractions. The purities of the individual exclusive processes will still be different, but the use of the dedicated graphite target for the background subtraction automatically corrects for such differences in a model-independent way. The use of a multi-variate selection allows an easy variation of the fixed efficiency, as shown in Fig. 4. As an example, Tab. II illustrates the results obtained by imposing the lowest efficiency achieved among individual channels in Tab. I.

C. Achievable statistics

In the following we will assume an overall fiducial mass of 5 tons for the CH₂ targets. This value is realistically achievable with the detector technology discussed in Sec. II and a relatively compact tracking volume around 45 m³ (without fiducial cuts), depending upon the specific configuration of the main STT parameters. The distributions of the generic kinematic variables $\vec{x} \equiv (x_1, x_2, \dots, x_n)$ in $\nu(\bar{\nu})$ -H CC interactions are obtained as:

$$N_H(\vec{x}) \equiv N_{\text{CH}_2}(\vec{x}) - N_C(\vec{x}) \times \frac{M_{C/\text{CH}_2}}{M_C} \quad (11)$$

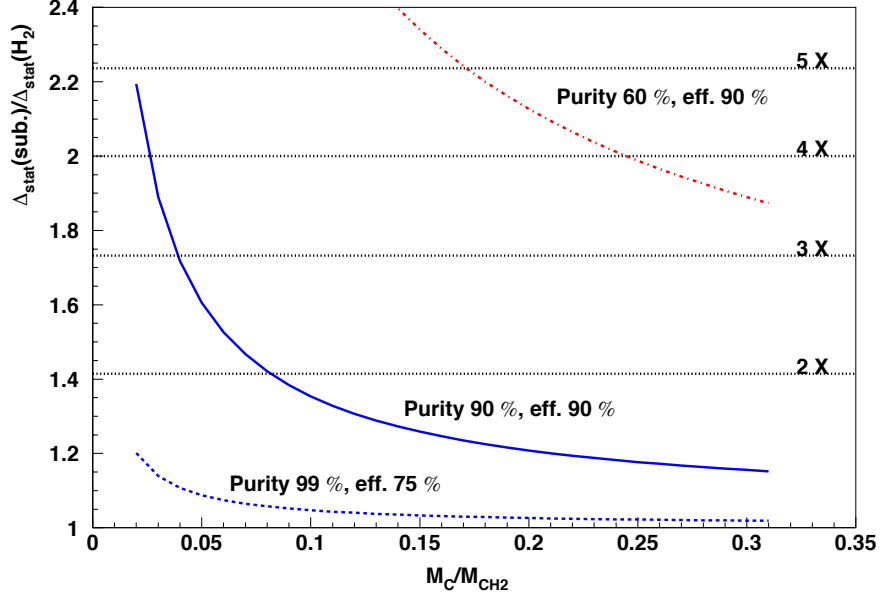


FIG. 7. Ratio between the relative statistical uncertainty Δ_{stat} on the H sample obtained after the C background subtraction and the corresponding ideal one from a pure H_2 sample of the same size, as a function of the ratio between the fiducial masses of the graphite and CH_2 targets, M_C/M_{CH_2} . The curves for a H purity of 90% (solid line) and 60% (dashed-dotted line) and 90% efficiency, as well as for a 99% purity and a 75% efficiency (dashed line) are shown to illustrate the impact of the kinematic selection. See text for details.

where N_{CH_2} and N_C are the data from the CH_2 plastic and graphite (C) targets. The interactions from this latter are normalized by the ratio between the total fiducial masses of C within the graphite and CH_2 targets, M_C/M_{CH_2} . The subtraction in Eq.(11) is performed after all the selection cuts, including the kinematic analysis described in Sec. III and resulting in the purities and efficiencies summarized in Tab. I. Practical considerations require the graphite targets to be smaller than the actual amount of C inside the CH_2 plastic, thus resulting in a statistical penalty associated with the subtraction procedure. Figure 7 illustrates how the total statistical uncertainty on N_H from Eq.(11) compares to the ideal one expected from a pure H_2 sample equivalent to the statistics of H interactions within CH_2 . For a given efficiency, the purity of the H samples achievable by the kinematic selection is crucial for the feasibility of this technique. Our analysis suggests that a fiducial mass for the graphite targets in the range 500-600 kg (i.e. $M_C/M_{\text{CH}_2} \sim 0.1$ -0.12) provides a reasonable compromise with a statistical penalty around 30%. We note that this statistical penalty can be further reduced by analytically smoothing the measured distributions from the graphite target and/or by using a tighter kinematic selection, as illustrated in Tab. II and Fig. 7.

As an example of application of our technique, we consider the neutrino and antineutrino beam spectra expected in the LBNF project. To this end, we assume a nominal beam power of 1.2 MW with 1.1×10^{21} pot/year and a data taking time of 5+5 years with the default low-energy neutrino and antineutrino beams [10, 30]. Table III summarizes the total number of events expected for the various topologies and targets. An interesting option available at LBNF is a high-energy beam optimized to detect the ν_τ appearance from neutrino oscillations in the far detector, which would result in an increase by a factor 2.4 of the $\nu(\bar{\nu})$ -H rates,

| CC process | CH ₂ target | H target | CH ₂ selected | C bkgnd | H selected |
|--------------------------------------------------|------------------------|-----------|--------------------------|---------|------------|
| $\nu_{\mu}p \rightarrow \mu^{-}p\pi^{+}$ | 5,615,000 | 2,453,000 | 2,305,000 | 115,000 | 2,190,000 |
| $\nu_{\mu}p \rightarrow \mu^{-}p\pi^{+}X$ | 11,444,000 | 955,000 | 877,000 | 61,000 | 816,000 |
| $\nu_{\mu}p \rightarrow \mu^{-}n\pi^{+}\pi^{+}X$ | 3,533,000 | 183,000 | 158,000 | 48,000 | 110,000 |
| ν_{μ} CC inclusive | 34,900,000 | 3,591,000 | 3,340,000 | 224,000 | 3,116,000 |
| $\bar{\nu}_{\mu}p \rightarrow \mu^{+}n$ | 4,450,000 | 1,688,000 | 1,274,000 | 255,000 | 1,019,000 |
| $\bar{\nu}_{\mu}p \rightarrow \mu^{+}p\pi^{-}$ | 827,000 | 372,000 | 342,000 | 17,000 | 325,000 |
| $\bar{\nu}_{\mu}p \rightarrow \mu^{+}n\pi^{0}$ | 791,000 | 366,000 | 295,000 | 48,000 | 247,000 |
| $\bar{\nu}_{\mu}p \rightarrow \mu^{+}p\pi^{-}X$ | 2,270,000 | 176,000 | 153,000 | 9,000 | 144,000 |
| $\bar{\nu}_{\mu}p \rightarrow \mu^{+}n\pi\pi X$ | 2,324,000 | 280,000 | 220,000 | 35,000 | 185,000 |
| $\bar{\nu}_{\mu}$ CC inclusive | 13,000,000 | 2,882,000 | 2,284,000 | 364,000 | 1,920,000 |

TABLE III. Number of events expected in the selection of all the various processes on H with the default low energy (anti)neutrino beams available at the LBNF [1, 2], assuming 5+5 years of data taking with the neutrino and antineutrino beams. The first two columns (CH₂ and H targets) refer to the initial statistics, while the last three include all selection cuts described in this paper (Sec. III and Tab. I). For the CH₂ and C targets the numbers refer to the given final state topologies originated from either p or n interactions. The fifth column shows the total residual C background to be subtracted from the corresponding CH₂ selected samples. We use a ratio $M_C/M_{C/CH_2} = 0.12$ to measure the C backgrounds from the graphite targets. See the text for details.

combined with a much harder spectrum. It is conceivable to have a dedicated 2 year run with this high energy beam after the completion of the nominal data taking [10, 30]. By that time the planned upgrades of the beam intensity to a nominal power of 2.4 MW would more than double the available statistics.

IV. DISCUSSION

A. Systematic uncertainties

The kinematic analysis described in Sec. III B allows the identification of all the various $\nu(\bar{\nu})$ -H CC topologies within the CH₂ target with little residual backgrounds 5-20% from interactions on the carbon nucleus. This selection dramatically reduces not only the statistical uncertainty from the background subtraction procedure (Sec. III C), but also the impact of systematic uncertainties on the modeling of nuclear effects in carbon [3]. These latter are further suppressed by a model-independent background subtraction using the data obtained from the dedicated graphite target, which also provides a pure background sample to build the likelihood functions used in the selection. The CH₂ plastic can be considered as an effective tank filled with hydrogen, while the graphite represents the empty tank. This technique is similar to what is done in electron scattering experiments, in which a cryogenic tank is filled with a liquid H₂ target and special runs with the empty tank are taken for background subtraction⁵. The detector technology discussed in Sec. II is essential, since the CH₂ and C

⁵ One of the dominant systematic uncertainties in electron scattering experiments on hydrogen is typically given by the knowledge of the density/mass of the cryogenic target. Our technique for measuring $\nu(\bar{\nu})$ -H

| Process | Selection | NuWro | | GiBUU | | GENIE | |
|------------------------------------------------|---------------------------------------------|------------|--------|------------|--------|------------|--------|
| | | Efficiency | Purity | Efficiency | Purity | Efficiency | Purity |
| $\nu_{\mu}p \rightarrow \mu^{-}p\pi^{+}$ | $\ln \lambda^H + \ln \lambda_{\text{IN}}^H$ | 96% | 95% | | | 96% | 96% |
| | $R_{mH} \ \& \ p_{T\perp}^H$ | 93% | 86% | 93% | 84% | 93% | 91% |
| $\bar{\nu}_{\mu}p \rightarrow \mu^{+}p\pi^{-}$ | $\ln \lambda^H + \ln \lambda_{\text{IN}}^H$ | 94% | 95% | | | 94% | 98% |
| | $R_{mH} \ \& \ p_{T\perp}^H$ | 89% | 84% | 89% | 87% | 89% | 89% |

TABLE IV. Comparison of the efficiency and purity for the kinematic selection of H interactions from the CH₂ target (Sec. III B) with the NuWro [24], GiBUU [25], and GENIE [26] event generators. The same cuts on the likelihood ratios as in Tab. I are used. In all cases the likelihood functions are built from the default NuWro generator and are not recalculated when different generators are tested. See text for details.

targets are configured as thin layers spread out uniformly over the tracking volume, ensuring that the corresponding acceptance corrections are small and, most importantly, the same on average for both targets. We verified this latter condition with detailed detector simulations using the GEANT4 program [31]. We emphasize that the data from the graphite target automatically include all types of interactions, as well as reconstruction effects, relevant for our analysis. The impact of possible model dependencies through the acceptance corrections is therefore negligible, since they would appear as third order effects on the data-driven subtraction of small backgrounds.

The kinematic selection of the signal from ν_{μ} -H and $\bar{\nu}_{\mu}$ -H CC interactions described in Sec. III B relies upon the absence of nuclear effects – i.e. target proton at rest and no final state interactions – rather than on the specific kinematics of the interactions with the free nucleon. Uncertainties on these latter, including form factors and structure functions, therefore can affect the resulting efficiencies only as second order effects through the small acceptance corrections for the individual exclusive topologies. Furthermore, uncertainties related to the structure of the free nucleon would affect both signal and backgrounds and largely cancel in a selection entirely based upon the differences introduced by nuclear effects. We note that the relevant proton form factors and structure functions can be determined in a model-independent way from the measured Q^2 and x distributions, using the procedure described in details in Ref. [34].

Although the technique we propose is designed to be model-independent, in the absence of actual data from STT the efficiencies and purities listed in Tab. I are sensitive to the details of the interaction modeling implemented in the simulations. In order to estimate the impact of such effects, we repeat the event selection described in Sec. III B with three event generators: NuWro [24], GiBUU [25], and GENIE [26]. These generators use rather different assumptions for the modeling of (anti)neutrino-nucleus interactions – including both initial and final state nuclear effects – as outlined in Ref. [27]. To this end, we do not recalculate the likelihood functions but rather use the ones obtained from the default NuWro generator throughout. Given the differences among generators [27, 34], this assumption helps to understand the impact of potential discrepancies between data and simulations on the H selection. As shown in Tab. IV, our kinematic selection of H interactions from the CH₂ targets is rather stable and we obtain comparable efficiencies and purities with all the three

interactions allows a more precise knowledge of the actual target mass.

event generators. We emphasize that this test is only meant to estimate the degree to which we can rely upon the numbers in Tab. I, since the actual technique is entirely data-driven and all backgrounds and efficiencies will be directly determined from the measured interactions.

Reconstruction effects on the four-momenta of the final state particles can in principle degrade the kinematic selection. For this reason in our studies we used a realistic detector smearing and checked its consistency with GEANT4 and FLUKA simulations (Sec. III A). Furthermore, we validated the effects of the detector acceptance, smearing, and track reconstruction with NOMAD data [20], although the NOMAD detector had worse acceptance and granularity than the STT. We note that similar kinematic selections were successfully demonstrated by NOMAD ⁶ in more severe background conditions (rejections up to 10^5) in various published analyses [21–23], as well as in single track measurements of $\bar{\nu}_\mu$ QE and inverse muon decay [35].

The momentum scale of charged particles is calibrated with the mass peak of the large samples of reconstructed $K_0 \rightarrow \pi^+\pi^-$ decays [34]. In our study we assume the same energy scale uncertainty of 0.2% achieved by the NOMAD experiment using this technique [36]. We note that the STT would provide 25 time higher granularity than NOMAD and about 40 times higher K_0 statistics [34]. Similarly, the proton identification and reconstruction efficiency can be accurately calibrated with the large samples of $\Lambda \rightarrow p\pi^-$ decays available [34]. Both Λ and K_0 decays can be used to constrain the systematic uncertainty on the reconstruction of the track angles.

The use of a likelihood function in the kinematic analysis (Sec. III B) provides a simple way to vary the purity and efficiency of the selected samples (Fig. 4) to validate the background subtraction and the selection efficiencies through appropriate control samples.

B. Unique option for $\nu(\bar{\nu})$ -H CC interactions

The technique we propose does not have many practical alternatives for the experimental detection of high statistics samples of $\nu(\bar{\nu})$ -H CC interactions. The only technology ideally able to deliver more accurate measurements (considering both statistics and resolution) would be a dedicated magnetized liquid H₂ detector – either a bubble chamber or a time-projection chamber (TPC), surrounded by an electromagnetic calorimeter and a muon identifier – with a fiducial volume > 10 m³. However, modern safety requirements for underground experimental halls and related costs make this option extremely challenging. We note that even such liquid H₂ detectors cannot provide the unique capability of STT to incorporate a wide range of nuclear targets to be compared with H measurements within the same detector for the study of nuclear effects. Our technique represents an acceptable approximation to pure H₂ targets, since it can achieve relatively small dilution factors (Tab. I and Tab. II) using a stringent kinematic selection. Filling a large TPC with high pressure H₂ gas, besides safety/cost concerns, would result in an insufficient statistics for any sensible physics measurement ⁷. The use of a plastic scintillator target cannot deliver the precision required for the detection of $\nu(\bar{\nu})$ -H interactions via subtraction with a graphite target. In addition to the smaller hydrogen content (CH vs. CH₂), the coarser vertex, angular, and momentum resolution achievable introduce larger systematic uncertainties in the location of $\nu(\bar{\nu})$ -H interactions and higher

⁶ The higher neutrino energy in NOMAD implies higher backgrounds and more difficult kinematic selections for low multiplicity processes like RES and QE compared to our case study. Furthermore, the lowest usable energy in NOMAD was about 5 GeV, which is reasonably close to the spectra expected at LBNF.

⁷ A total TPC volume of about 2,500 m³ filled with H₂ gas at 10 atm would be required to match the statistics achievable with our technique.

backgrounds from the kinematic selection (Fig. 7). Furthermore, the many impurities from glue, fibers, coatings, etc. make the subtraction of nuclear components problematic in relation to the small H content of about 7%.

C. Physics Measurements

The availability of high statistics samples of $\nu(\bar{\nu})$ -H CC interactions can represent a significant advancement for neutrino scattering physics, as well as for long-baseline oscillation experiments. In this section we outline some of the key physics measurements [10, 30, 34].

The limited knowledge of the (anti)neutrino flux has always been a bottleneck for accelerator based neutrino experiments. The exclusive $\nu_{\mu}p \rightarrow \mu^{-}p\pi^{+}$, $\bar{\nu}_{\mu}p \rightarrow \mu^{+}p\pi^{-}$, and $\bar{\nu}_{\mu}p \rightarrow \mu^{+}n$ processes on hydrogen with small energy transfer ν offer a measurement of relative fluxes as a function of energy with little hadronic uncertainties. To this end, the use of the samples described in Sec. III C allows a determination of the ν_{μ} and $\bar{\nu}_{\mu}$ relative flux to a precision better than 1% [34], not achievable with other techniques using nuclear targets. The measurement of the $\bar{\nu}_{\mu}p \rightarrow \mu^{+}n$ QE interactions on H at small momentum transfer Q also provides an absolute measurement of the $\bar{\nu}_{\mu}$ flux, since the corresponding cross-section in the limit $Q \rightarrow 0$ is a constant known to high accuracy from neutron β decay [34].

A comparison of $\nu(\bar{\nu})$ -H CC interactions with the corresponding ones from nuclear targets within the same detector provides a direct measurement/constraint of nuclear effects, which typically result in a substantial smearing of the observed interactions. This study can be performed with both inclusive CC events and with various exclusive topologies. Constraining the nuclear smearing from initial and final state interactions is required to reduce the uncertainties in the unfolding of data collected from heavy targets and to calibrate the reconstructed neutrino energy scale.

The possibility to control the (anti)neutrino target and the input fluxes to an unprecedented accuracy [34] would open up a sensible program of precision tests of fundamental interactions [10, 30]. An example is given by the Adler sum rule [37], $S_A = \int_0^1 dx/x (F_2^{\bar{\nu}p} - F_2^{\nu p}) = 2$, which is based upon current algebra and was tested only by BEBC [38] with a few thousand events. Similarly, by exploiting the isospin symmetry $F_2^{\nu n} = F_2^{\nu p}$, we can obtain a model-independent measurement of the free neutron structure functions, as well as a measurement of the large x behavior of the d/u quark ratio [39]. These measurements can also be used for precision tests of the isospin (charge) symmetry and would help to elucidate the flavor structure of the nucleon [40].

V. SUMMARY

We presented a novel approach to achieve precision measurements of $\nu(\bar{\nu})$ -hydrogen CC interactions via subtraction between dedicated CH₂ plastic and graphite (pure C) targets, embedded within a low density tracker allowing a control of the configuration, chemical composition, size, and mass of the targets similar to electron scattering experiments. We used a kinematic selection to reduce backgrounds from the carbon nucleus in the CH₂ measurements to about 5-20%, depending upon the specific event topology considered. The measurement of this background is entirely data-driven by subtracting it using the corresponding graphite target measurements.

The availability of large control samples of $\nu(\bar{\nu})$ -H CC interactions is a necessary condition for any program of precision measurements with (anti)neutrino interactions in order to constrain nuclear effects, as well as to achieve the accuracies required by next-generation long-baseline oscillation experiments. The simple and safe approach we proposed appears to be a viable alternative to liquid H₂ detectors and a realistic opportunity to obtain such high statistics samples, since safety and practical arguments make other techniques unfeasible.

The use of exclusive $\nu(\bar{\nu})$ -H CC processes allows a determination of ν_μ and $\bar{\nu}_\mu$ relative fluxes in conventional wide band (anti)neutrino beams to a precision better than 1%, which cannot be achieved by other known techniques. In combination with nuclear targets integrated within the same detector, $\nu(\bar{\nu})$ -H CC interactions provide a direct measurement of nuclear effects resulting in the smearing of the observed $\nu(\bar{\nu})$ -nucleus interactions. Finally, they represent the key to access a sensible program of precision tests of fundamental interactions and of the structure of nucleons and nuclei.

ACKNOWLEDGMENTS

The authors express their gratitude to the LBNE and DUNE experiments for the use of some detector simulation tools. We thank L. Camilleri, R. Ent, X. Lu, and X. Qian for fruitful discussions. We thank F. Ferraro, L. Di Noto, P. Sala, and M. Torti for providing the reconstruction smearing of n and π^0 with the FLUKA simulation package. This work was supported by Grant No. [de-sc0010073](#) from the Department of Energy, USA.

-
- [1] R. Acciarri *et al.* (DUNE), (2015), [arXiv:1512.06148 \[physics.ins-det\]](#).
 - [2] R. Acciarri *et al.* (DUNE), (2016), [arXiv:1601.02984 \[physics.ins-det\]](#).
 - [3] L. Alvarez-Ruso *et al.*, *Prog. Part. Nucl. Phys.* **100**, 1 (2018), [arXiv:1706.03621 \[hep-ph\]](#).
 - [4] S. J. Barish *et al.*, *Phys. Rev.* **D19**, 2521 (1979).
 - [5] N. J. Baker, P. L. Connolly, S. A. Kahn, M. J. Murtagh, R. B. Palmer, N. P. Samios, and M. Tanaka, *Phys. Rev.* **D25**, 617 (1982).
 - [6] G. T. Jones *et al.* (Birmingham-CERN-Imperial Coll-Munich (MPI)-Oxford-Univ Coll London), *Z. Phys.* **C54**, 45 (1992).
 - [7] G. T. Jones *et al.* (WA21), *Z. Phys.* **C46**, 25 (1990).
 - [8] J. Bell *et al.*, *Phys. Rev.* **D19**, 1 (1979).
 - [9] M. Derrick *et al.*, *Phys. Rev.* **D25**, 624 (1982).
 - [10] P. Bernardini *et al.*, Proposal accepted for the European Particle Physics Strategy Update 2018-2020, <https://indico.cern.ch/event/765096/contributions/3295805/>.
 - [11] M. Adinolfi *et al.*, *Nucl. Instrum. Meth.* **A482**, 364 (2002).
 - [12] A. Sergi, *Proceedings, 2nd International Conference on Technology and Instrumentation in Particle Physics 2011: Chicago, Illinois, 9-14 Jun 2011*, *Phys. Procedia* **37**, 530 (2012).
 - [13] M. Anelli *et al.* (SHiP), (2015), [arXiv:1504.04956 \[physics.ins-det\]](#).
 - [14] H. Nishiguchi *et al.*, *Proceedings, 14th Vienna Conference on Instrumentation (VCI 2016): Vienna, Austria, February 15-19, 2016*, *Nucl. Instrum. Meth.* **A845**, 269 (2017).
 - [15] M. Lee, *Nuclear and Particle Physics Proceedings* **273-275**, 2530 (2016), 37th International Conference on High Energy Physics (ICHEP).
 - [16] P. Gianotti *et al.*, in *Proceedings, 3rd International Conference on Advancements in Nuclear*

- Instrumentation Measurement Methods and their Applications (ANIMMA 2013): Marseille, France, June 23-27, 2013* (2013) arXiv:1307.4537 [physics.ins-det].
- [17] S. A. Kulagin and R. Petti, *Nucl. Phys.* **A765**, 126 (2006), arXiv:hep-ph/0412425 [hep-ph].
 - [18] S. A. Kulagin and R. Petti, *Phys. Rev.* **D76**, 094023 (2007), arXiv:hep-ph/0703033 [HEP-PH].
 - [19] S. A. Kulagin and R. Petti, *Phys. Rev.* **C90**, 045204 (2014), arXiv:1405.2529 [hep-ph].
 - [20] J. Altegoer *et al.* (NOMAD), *Nucl. Instrum. Meth.* **A404**, 96 (1998).
 - [21] P. Astier *et al.* (NOMAD), *Nucl. Phys.* **B611**, 3 (2001), arXiv:hep-ex/0106102 [hep-ex].
 - [22] D. Naumov *et al.* (NOMAD), *Nucl. Phys.* **B700**, 51 (2004), arXiv:hep-ex/0409037 [hep-ex].
 - [23] P. Astier *et al.* (NOMAD), *Phys. Lett.* **B483**, 387 (2000).
 - [24] C. Juszczak, J. A. Nowak, and J. T. Sobczyk, *NuInt05, proceedings of the 4th International Workshop on Neutrino-Nucleus Interactions in the Few-GeV Region, Okayama, Japan, 26-29 September 2005*, *Nucl. Phys. Proc. Suppl.* **159**, 211 (2006), [,211(2005)], arXiv:hep-ph/0512365 [hep-ph].
 - [25] O. Buss, T. Gaitanos, K. Gallmeister, H. van Hees, M. Kaskulov, O. Lalakulich, A. B. Larionov, T. Leitner, J. Weil, and U. Mosel, *Phys. Rept.* **512**, 1 (2012), arXiv:1106.1344 [hep-ph].
 - [26] C. Andreopoulos *et al.*, *Nucl. Instrum. Meth.* **A614**, 87 (2010), arXiv:0905.2517 [hep-ph].
 - [27] U. Mosel, (2019), arXiv:1904.11506 [hep-ex].
 - [28] X. G. Lu *et al.* (MINERvA), *Phys. Rev. Lett.* **121**, 022504 (2018), arXiv:1805.05486 [hep-ex].
 - [29] K. Abe *et al.* (T2K), *Phys. Rev.* **D98**, 032003 (2018), arXiv:1802.05078 [hep-ex].
 - [30] R. Petti, Workshop on Near Detector Physics at Neutrino Experiments, CERN, 18-22 June 2018, <https://indico.cern.ch/event/721473/contributions/3034869/>.
 - [31] S. Agostinelli *et al.* (GEANT4), *Nucl. Instrum. Meth.* **A506**, 250 (2003).
 - [32] G. Battistoni *et al.*, *Annals of Nuclear Energy* **82**, 10 (2015).
 - [33] X. G. Lu, D. Coplowe, R. Shah, G. Barr, D. Wark, and A. Weber, *Phys. Rev.* **D92**, 051302 (2015), arXiv:1507.00967 [hep-ex].
 - [34] H. Duyang, B. Guo, S. R. Mishra, and R. Petti, *Phys. Lett.* **B795**, 424 (2019), arXiv:1902.09480 [hep-ph].
 - [35] V. Lyubushkin *et al.* (NOMAD), *Eur. Phys. J.* **C63**, 355 (2009), arXiv:0812.4543 [hep-ex].
 - [36] Q. Wu *et al.* (NOMAD), *Phys. Lett.* **B660**, 19 (2008), arXiv:0711.1183 [hep-ex].
 - [37] S. L. Adler, *Phys. Rev.* **135**, B963 (1964).
 - [38] D. Allasia *et al.*, *Z. Phys.* **C28**, 321 (1985).
 - [39] S. I. Alekhin, S. A. Kulagin, and R. Petti, *Phys. Rev.* **D96**, 054005 (2017), arXiv:1704.00204 [nucl-th].
 - [40] S. Alekhin, J. Blmlein, S. Kulagin, S.-O. Moch, and R. Petti, in *26th International Workshop on Deep Inelastic Scattering and Related Subjects (DIS 2018) Port Island, Kobe, Japan, April 16-20, 2018* (2018) arXiv:1808.06871 [hep-ph].